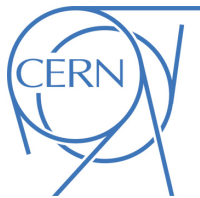




## ATLAS NOTE

ATLAS-CONF-2016-057

3rd August 2016



# Search for massive supersymmetric particles in multi-jet final states produced in $pp$ collisions at $\sqrt{s} = 13$ TeV using the ATLAS detector at the LHC

The ATLAS Collaboration

## Abstract

Results of a search for supersymmetric gluino pair productions with subsequent  $R$ -parity-violating decays to quarks are presented. This search uses  $14.8 \text{ fb}^{-1}$  of data collected by the ATLAS detector in proton-proton collisions with a center-of-mass energy of  $\sqrt{s} = 13$  TeV at the LHC. The analysis is performed using both a requirement on the number of jets and the number of jets tagged as containing a  $b$ -hadron as well as a topological observable formed from the scalar sum of large-radius jet masses in the event. No significant deviation is observed from the expected Standard Model backgrounds. For a model where the gluino decays through an intermediate neutralino which, in turn, decays to three quarks, gluino masses ( $m_{\tilde{g}}$ ) below 1000-1550 GeV are excluded depending on the neutralino mass. Gluinos decaying directly to three quarks are excluded for  $m_{\tilde{g}} < 1080$  GeV.

# 1 Introduction

Supersymmetry (SUSY) [1–6] is a theoretical extension of the Standard Model (SM) which fundamentally relates fermions and bosons. It is an alluring theoretical possibility given its potential to solve the naturalness problem [7, 8].

This note presents a search for  $R$ -parity-violating (RPV) [9–14] supersymmetric gluino pair production with subsequent decays to quarks in events with many jets using  $14.8 \text{ fb}^{-1}$  of  $pp$  collision data at  $\sqrt{s} = 13 \text{ TeV}$  collected by the ATLAS detector in 2015 and 2016. In supersymmetry, the RPV component of a generic superpotential can be written as [15, 16]:

$$W_{RPV} = \frac{1}{2} \lambda_{ijk} L_i L_j \bar{E}_k + \lambda'_{ijk} L_i Q_j \bar{D}_k + \frac{1}{2} \lambda''_{ijk} \bar{U}_i \bar{D}_j \bar{D}_k + \kappa_i L_i H_2, \quad (1)$$

where  $i, j, k = 1, 2, 3$  are generation indices. The generation indices are sometimes omitted in the discussions that follow if the statement being made is not specific to any generation. The first three terms in Eq. (1) are often referred to as the trilinear couplings, whereas the last term is referred to as bilinear. The  $L_i$ ,  $Q_i$  represent the lepton and quark  $SU(2)_L$  doublet superfields, whereas  $H_2$  represents the Higgs superfield. The  $\bar{E}_j$ ,  $\bar{D}_j$ , and  $\bar{U}_j$  are the charged lepton, down-type quark, and up-type quark  $SU(2)_L$  singlet superfields, respectively. The couplings for each term are given by  $\lambda$ ,  $\lambda'$ , and  $\lambda''$ , and  $\kappa$  is a dimensional mass parameter. In the benchmark models considered in this search, only the baryon-number-violating coupling  $\lambda''_{ijk}$  is non-zero, in order to protect the proton from rapid decay. Because of the structure of Eq. (1), scenarios in which only  $\lambda''_{ijk} \neq 0$  are often referred to as UDD scenarios. The diagrams shown in Figure 1 represent the benchmark processes used in the optimization and design of the search presented in this note. In the gluino direct decay model (Figure 1(a)), the gluino directly decays to three quarks via the RPV UDD coupling  $\lambda''$ , leading to six quarks in the final state of gluino pair production. In the gluino cascade decay model (Figure 1(b)), the gluino decays to two quarks and a neutralino, which, in turn, decays to three quarks via the RPV UDD coupling  $\lambda''$ , resulting in ten quarks in the final state of gluino pair production. Events produced in these processes typically have a high multiplicity of reconstructed jets as well as complex event topology. In signal models considered in this search, the production of the gluino pair is assumed to be independent of the value of  $\lambda''$ . All possible  $\lambda''$  flavor combinations given by the structure of Eq. 1 are assumed to proceed with equal probability, and decays of the gluino and neutralino are assumed to be prompt. Under this configuration, a significant portion of signal events contain at least one bottom or top quark. Other models of the RPV UDD scenario, such as the Minimum Flavor Violation model [17, 18], also predict that the gluino decays preferably to final states with third generation quarks. These theoretical arguments motivate the introduction of  $b$ -tagging requirements to the search.

This analysis is an update to previous ATLAS searches for signals arising from RPV UDD scenarios [19, 20] performed with data taken during LHC Run-1. The search strategy follows closely the one implemented by the ATLAS Collaboration using LHC Run-1 data at  $\sqrt{s} = 8 \text{ TeV}$  in Ref. [20], which has excluded a gluino with mass up to 917 GeV in the gluino direct decay model, and a gluino with mass up to 1 TeV for a neutralino mass of 500 GeV in the gluino cascade decay model.

In a recent publication [21], the CMS collaboration also set a limit on the gluino mass up to 1.03 TeV in a RPV UDD scenario where the gluino exclusively decays to a final state of a top quark, a bottom quark and a strange quark, using  $\sqrt{s} = 8 \text{ TeV}$   $pp$  collision data.

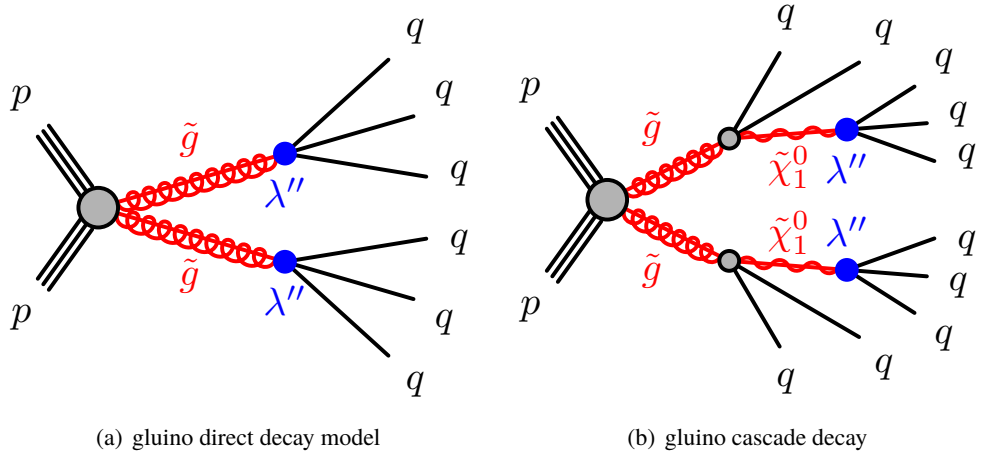


Figure 1: Diagrams for the benchmark processes considered for this analysis. The black lines represent Standard Model particles, the red lines represent SUSY partners, the gray shaded circles represent effective vertices that include off-shell propagators (e.g. heavy squarks coupling to a  $\tilde{\chi}_1^0$  neutralino and a quark), and the blue solid circles represent effective RPV vertices allowed by the baryon-number-violating  $\lambda''$  couplings with off-shell propagators (e.g. heavy squarks coupling to two quarks).

## 2 ATLAS detector

The ATLAS detector [22] covers almost the whole solid angle around the collision point with layers of tracking detectors, calorimeters and muon chambers. For the measurements presented in this note, the calorimeters are of particular importance. The inner detector, immersed in a magnetic field provided by a solenoid, has full coverage in  $\phi$  and covers the pseudorapidity range  $|\eta| < 2.5$ <sup>1</sup>. It consists of a silicon pixel detector, a silicon microstrip detector and a transition radiation straw-tube tracker. The innermost pixel layer [23] was added between Run-1 and Run-2 of the LHC, around a new thinner (radius of 25 mm) beam pipe. In the pseudorapidity region  $|\eta| < 3.2$ , high granularity lead liquid-argon (LAr) electromagnetic (EM) sampling calorimeters are used. A steel-scintillator tile calorimeter provides hadronic calorimetry coverage over  $|\eta| < 1.7$ . The end-cap and forward regions, spanning  $1.5 < |\eta| < 4.9$ , are instrumented with LAr calorimetry for both EM and hadronic measurements. The muon spectrometer surrounds these calorimeters, and comprises a system of precision tracking chambers and trigger detectors with three large toroids, each consisting of eight coils providing the magnetic field for the muon detectors. A two-level trigger system is used to select events [24]. The first-level trigger is implemented in hardware and uses a subset of the detector information. This is followed by the software-based High-Level Trigger, which can run offline reconstruction and calibration software, reducing the event rate to about 1 kHz.

<sup>1</sup> ATLAS uses a right-handed coordinate system with its origin at the nominal interaction point in the center of the detector and the  $z$ -axis along the beam direction. The  $x$ -axis points toward the center of the LHC ring, and the  $y$ -axis points upward. Cylindrical coordinates  $(r, \phi)$  are used in the transverse plane,  $\phi$  being the azimuthal angle around the beam pipe. The pseudorapidity  $\eta$  is defined in terms of the polar angle  $\theta$  by  $\eta \equiv -\ln[\tan(\theta/2)]$ .

### 3 Simulation samples

Signal samples are produced covering a wide range of gluino and neutralino masses. In the gluino direct decay model, the gluino mass ( $m_{\tilde{g}}$ ) is varied from 900 GeV to 1800 GeV. In the case of the cascade decays, for each gluino mass (1000 GeV to 1.9 TeV), separate samples are generated with multiple neutralino masses ( $m_{\tilde{\chi}_1^0}$ ) ranging from 50 GeV to 1.65 TeV. In each case,  $m_{\tilde{\chi}_1^0} < m_{\tilde{g}}$ . Signal samples are generated at the leading order (LO) using the MadGraph5\_aMC@NLO v2.3.3 event generator [25] interfaced to PYTHIA 8.186 [26]. The A14 [27] tune is used together with the NNPDF2.3LO [28] parton distribution function (PDF) set. The EvtGen v1.2.0 program [29] is used to describe the properties of the  $b$ - and  $c$ - hadron decays in the signal samples and the background samples except those produced with SHERPA [30]. The signal production cross-sections are calculated at next-to-leading order (NLO) in the strong coupling constant, adding the resummation of soft gluon emission at next-to-leading-logarithmic accuracy (NLO+NLL) [31–35]. The nominal cross-section and its uncertainty are taken from Ref. [36]. Cross-sections are evaluated assuming masses of 450 TeV for the light-flavour squarks in case of gluino pair production. In the simulation, the total widths of gluino and neutralino are set to be 1 GeV, effectively making their decays prompt.

While a data-driven method is used to estimate the background, simulated events are used to establish, test and validate the methodology of the analysis. Therefore, simulation is not required to precisely describe the background, but it should be sufficiently similar that the strategy can be tested before applying it to data. Multi-jet events constitute the dominant background in the search region, with small contributions from top-quark pair-production ( $t\bar{t}$ ). Contributions from  $\gamma$  + jets,  $W$  + jets,  $Z$  + jets, single-top quark, and diboson background processes are negligible from simulation.

The multi-jet background is generated with PYTHIA 8.186 using the A14 tune and the NNPDF2.3LO parton distribution functions. SHERPA multi-jet samples are also generated and tested for the background estimation. Matrix elements are calculated with up to 3 partons at LO and merged with the SHERPA parton shower [37] using the ME+PS@LO prescription [38]. The CT10 PDF set [39] is used in conjunction with dedicated parton shower tuning developed by the Sherpa authors.

For the generation of fully hadronic decaying  $t\bar{t}$  events, the POWHEG-Box v2 [40] generator is used with the CT10 PDF set. The parton shower, fragmentation, and the underlying event are simulated using PYTHIA 6.428 [41] with the CTEQ6L1 PDF set [42] and the corresponding Perugia 2012 tune (P2012) [43].

The effect of additional  $pp$  interactions per bunch crossing (“pile-up”) as a function of the instantaneous luminosity is taken into account by overlaying simulated minimum-bias events according to the observed distribution of the number of pile-up interactions in data. All Monte-Carlo (MC) simulated background samples are passed through a full GEANT4 [44] simulation of the ATLAS detector [45]. The signal samples are passed through a fast detector simulation based on a parameterization of the performance of the ATLAS electromagnetic and hadronic calorimeters [46] and on GEANT4 elsewhere.

### 4 Event selection

The data used here were recorded in 2015 and 2016, with the LHC operating at a center-of-mass energy of  $\sqrt{s} = 13$  TeV. All detector elements are required to be fully operational. The integrated luminosity is measured to be  $3.2 \text{ fb}^{-1}$  and  $11.6 \text{ fb}^{-1}$ , for the 2015 data set and 2016 data set, respectively. The luminosity measurement was calibrated during dedicated beam-separation scans, using the same methodology as that

described in [47]. The uncertainty of this measurement is found to be 2.1% for 2015 data, and 3.7% for 2016 data. In this analysis, the 2015 and 2016 data sets are combined and treated as a single data set, corresponding to a total integrated luminosity of  $14.8 \text{ fb}^{-1}$ .

The events used in this search are selected using a large- $R$  jet trigger, which requires at least one anti- $k_t$  jet [48] with a radius of 1.0 and a  $p_T > 420 \text{ GeV}$ .

Events are required to have a primary vertex with at least two associated tracks with  $p_T$  above 0.4 GeV. The primary vertex assigned to the hard-scattering collision is the one with the highest  $\sum_{\text{track}} p_T^2$ , where the scalar sum of track  $p_T^2$  is taken over all tracks associated with that vertex.

Since the signal process is characterised by the presence of many quarks, the analysis only considers jets in the events. Jets are reconstructed from three-dimensional topological clusters of energy deposits in the calorimeter calibrated at the EM scale [49], using the anti- $k_t$  algorithm with two different radius parameters of  $R = 1.0$  and  $R = 0.4$ , hereafter referred to as large- $R$  jets and small- $R$  jets, respectively. The four-momenta of the jets are calculated as the sum of the four-momenta of the clusters, which are assumed to be massless. For the large- $R$  jets, the original constituents are calibrated using the local cluster weighting algorithm [50] and reclustered using the longitudinally-invariant  $k_t$  algorithm [51] with a radius parameter of  $R_{\text{sub-jet}} = 0.2$ , to form a collection of sub-jets. A sub-jet is discarded if it carries less than 5% of the  $p_T$  of the original jet. The constituents in the remaining sub-jets are then used to recalculate the large- $R$  jet four-momenta, and the jet energy and mass are further calibrated to particle level using correction factors derived from simulation [52]. The resulting “trimmed” [53] large- $R$  jets are required to have  $p_T > 200 \text{ GeV}$  and  $|\eta| < 2.0$ . The analysis selects events with at least three large- $R$  jets and requires the  $p_T$  of leading large- $R$  jet to be greater than 440 GeV so that the trigger is fully efficient with respect to the analysis selection. Events with three large- $R$  jets are used to derive jet mass templates. Events with higher large- $R$  jet multiplicity are used to validate background estimation performance and probe the existence of Beyond SM (BSM) signals. The small- $R$  jets are corrected for pile-up contributions and are then calibrated to the particle level using simulation followed by a correction based on in-situ measurements [54].

The identification of jets containing  $b$ -hadrons is based on the small- $R$  jet with  $p_T > 50 \text{ GeV}$  and  $|\eta| < 2.5$  and a multivariate tagging algorithm [55, 56]. This algorithm is applied to a set of tracks with loose impact parameter constraints in a region of interest around each jet axis to enable the reconstruction of the  $b$ -hadron decay vertex. The  $b$ -tagging requirements result in an efficiency of 70% for jets containing  $b$ -hadrons, as determined in a sample of simulated  $t\bar{t}$  events [56]. A small- $R$  jet passing the  $b$ -tagging requirement is considered as a  $b$ -jet. The events selected in the analysis are further divided to a  $b$ -tag sample where at least one  $b$ -jet is present in the event, and a  $b$ -veto sample where no  $b$ -jet is present in the event. Events selected without a  $b$ -tagging requirement are referred to as **inclusive** events.

## 5 Analysis strategy

The analysis uses a topological observable, the total jet mass variable,  $M_J^\Sigma$ , as the primary discriminating variable to separate signal and background. The observable  $M_J^\Sigma$  [57–59] is defined as the scalar sum of

the masses of the four leading large- $R$  jets reconstructed with a radius parameter  $R = 1.0$ ,  $p_T > 200$  GeV and  $|\eta| < 2.0$ ,

$$M_J^\Sigma = \sum_{\substack{p_T > 200 \text{ GeV} \\ |\eta| \leq 2.0}}^4 m^{\text{jet}}. \quad (2)$$

This observable was used for the first time in the  $\sqrt{s} = 8$  TeV search by the ATLAS Collaboration for events with many jets and missing transverse momentum [60] and provides significant sensitivity for very high-mass gluinos. It was also used in the search by the ATLAS Collaboration for RPV SUSY in events with many jets using the Run-1 LHC data [20]. Here, the four leading jets in the event are used, as they cover a significant portion of the central region of the calorimeter, and are very likely to capture most signal quarks.

Simulation studies show that  $M_J^\Sigma$  provides greater sensitivity than variables such as  $H_T$  or the scalar sum of jet  $p_T$ . The masses contain angular information about the events, whereas a variable like  $H_T$  simply describes the energy (or transverse momentum) in the event. A large  $M_J^\Sigma$  implies not only high energy of the multi-jet system, but also rich angular structure. Previous studies with the Monte Carlo generators have demonstrated the power of the  $M_J^\Sigma$  variable in the high-multiplicity events that this analysis targets [57, 58]. Figure 2(a) presents examples of the discrimination that the  $M_J^\Sigma$  observable provides between the background (represented here by SHERPA and PYTHIA 8.186 multi-jet MC simulation) and several signal samples, as well as the comparison of the data to the Monte Carlo multi-jet background.

Another discriminating variable that is independent of  $M_J^\Sigma$  is necessary in order to define suitable control and validation regions where the background estimation can be studied and tested. The signal is characterized by a higher rate of central jet events as compared to the primary multi-jet background. This is expected due to the difference in the production processes that is predominantly  $s$ -channel for the signal, while the background can also be produced through  $u$ - and  $t$ -channel processes. Figure 2(b) shows the distribution of the pseudorapidity difference between the two leading large- $R$  jets,  $|\Delta\eta_{12}|$  for several signal and background Monte Carlo samples, as well as data. A high  $|\Delta\eta_{12}|$  requirement can be applied to establish a control region or a validation region where the potential signal contamination needs to be suppressed.

The use of  $M_J^\Sigma$  in this analysis provides an opportunity to employ the fully data-driven jet mass *template method* to estimate the background contribution in signal regions. The jet mass template method is discussed in Ref. [59], and its first experimental implementation is described in Ref. [20] (the Run-1 analysis). In this method, single jet mass templates are extracted from signal-depleted control regions, or *training samples*. These jet mass templates are created in bins of jet  $p_T$  and  $\eta$ . They provide a *probability density function* that describes the relative probability for a jet with a given  $p_T$  and  $\eta$  to have a certain mass. This method assumes that jet mass templates only depend on jet  $p_T$  and  $\eta$  and are the same between control regions and signal regions. A sample where the background  $M_J^\Sigma$  distribution needs to be estimated, such as a validation region or a signal region, is referred to as the *kinematic sample*. The only information used is the jet  $p_T$  and  $\eta$ , which are inputs to the templates. For each jet in the kinematic sample, the  $p_T$ - $\eta$  dependent jet mass template is sampled to generate a random jet mass. A  $M_J^\Sigma$  distribution can be constructed from the randomized jet masses of the kinematic sample. This procedure is referred to as “dressing”, and the resulting sample is referred to as a *dressed sample*. If jet mass templates are created from a control sample of background events and the number of events in the kinematic sample is

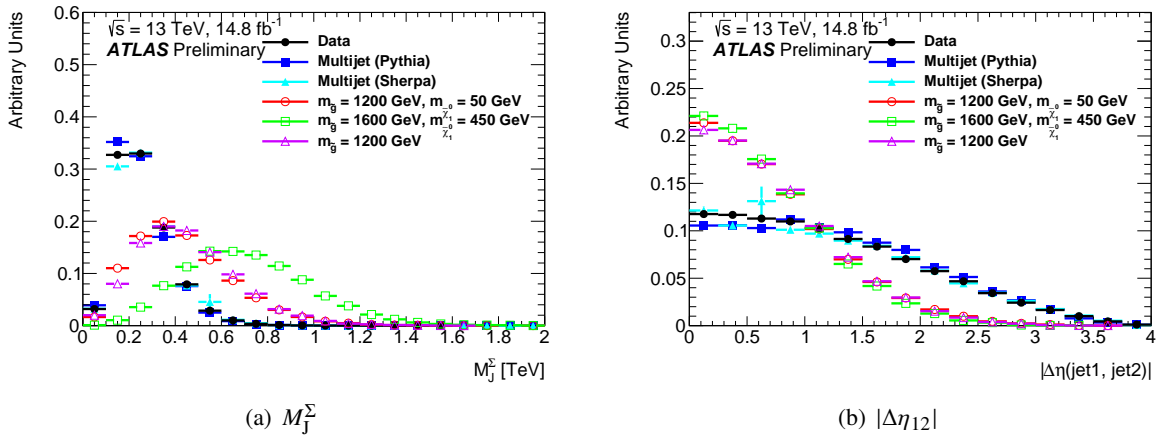


Figure 2: Comparison between signal sample and background dominant data control sample for (a) the scalar sum of the masses of the four leading large- $R$  jets  $M_J^\Sigma$  and (b) the difference in pseudorapidity between the two leading large- $R$  jets  $|\Delta\eta_{12}|$ . Several typical signal points are shown, as well as the distributions obtained from the data. All distributions are normalized to the same area. The selection requires four or more jets, is inclusive in  $|\Delta\eta_{12}|$  and has no  $b$ -tagging requirements.

sufficiently large, then the  $M_J^\Sigma$  distribution constructed from randomized jet masses should reproduce the shape of the  $M_J^\Sigma$  distribution for the background.

This analysis adopts basically the same procedure employed in the Run-1 analysis [20] with two minor differences. First, the statistical fluctuations in the jet mass templates is propagated to the prediction of background yield in the signal region, and therefore considered as a systematic uncertainty of the jet mass template method, whereas the Run-1 analysis smoothed the jet mass templates with a Gaussian kernel technique. Second, the predicted  $M_J^\Sigma$  distribution is normalized to the observation in  $0.2 \text{ TeV} < M_J^\Sigma < 0.6 \text{ TeV}$ , whereas the Run-1 analysis did not introduce any normalization region, effectively normalizing the prediction to the observation in the entire  $M_J^\Sigma$  range. In the region of  $0.2 \text{ TeV} < M_J^\Sigma < 0.6 \text{ TeV}$ , contamination from signal models not yet excluded by the ATLAS Run-1 search [20] is negligible compared to the statistical uncertainty of background.

The selected events are divided into control, validation and signal regions, as summarized in Table 1. Control regions are defined with events that have three large- $R$  jets with  $p_T > 200 \text{ GeV}$ . Additional requirements on the number of large- $R$  jet with  $100 \text{ GeV} < p_T < 200 \text{ GeV}$  (soft large- $R$  jets) are used to separate control regions for events with different large- $R$  jet multiplicities. For events with four or more large- $R$  jets (4j events), two control regions with a common requirement of at least one soft large- $R$  jet being present are formed: one (3jCRb1\_4j) consists of  $b$ -tag events and requires  $|\Delta\eta_{12}| > 1.4$ , the other (3jCRb0\_4j) consists of  $b$ -veto events without requirement on  $|\Delta\eta_{12}|$ . For events with five or more large- $R$  jets (5j events), one single control region (3jCR\_5j) is defined by requiring the presence of at least two soft large- $R$  jets. Because of limited statistics of such events, this control region is not further divided based on number of  $b$ -jets. For each control region, a variable binning in jet  $p_T$  and  $\eta$  is chosen to ensure that every jet mass template has a sufficiently large number of jets.

Four overlapping signal regions (SRs) are considered in this analysis. All signal regions are required to have  $|\Delta\eta_{12}| < 1.4$ . The first set of signal regions does not require the presence of a  $b$ -jet and is used to test more generic BSM signals of pair-produced heavy particles cascade decaying to many quarks or gluons.

$N_{\text{jet}}$	b-tag		b-veto	inclusive	
	$ \Delta\eta_{12}  > 1.4$	$ \Delta\eta_{12}  < 1.4$	-	$ \Delta\eta_{12}  > 1.4$	$ \Delta\eta_{12}  < 1.4$
= 3	3jCRb1_4j	-	3jCRb0_4j	3jCR_5j	
$\geq 4$	4jVRb1	4jSRb1	-	4jVR	4jSR
$\geq 5$	5jVRb1	5jSRb1	-	5jVR	5jSR

Table 1: Control (CR), validation (VR), and signal (SR) regions used for the analysis.

Two selections on the large- $R$  jet multiplicity are used,  $N_{\text{jet}} \geq 4$  (4jSR) and  $N_{\text{jet}} \geq 5$  (5jSR). To further improve the sensitivity to the benchmark signal models of RPV UDD scenario, subsets of events in the 4jSR and 5jSR are selected by requiring the presence of at least one  $b$ -tagged small- $R$  jet. For each signal region, by reversing the  $|\Delta\eta_{12}|$  requirement, a validation region is defined, which is used to cross check the background estimation, thus validating the background prediction in the signal region.

The background estimation performance is first examined in the validation region, before the signal region is unblinded.

Three main systematic uncertainties associated with the jet mass template method are considered. First, the jet mass template is created from a statistically limited jet sample and therefore the jet mass template is subject to statistical fluctuation. In addition, the jet mass randomization is statistical. The following procedure is used to propagate these statistical uncertainties to the predicted background yield for a given  $M_j^\Sigma$  region. For each jet mass template, 1000 randomized templates are created by introducing bin-by-bin Poisson fluctuations to the template. These randomized templates are applied to the kinematic sample, generating 1000 randomized  $M_j^\Sigma$  distributions. The central value of the predicted  $M_j^\Sigma$  distribution is derived from the median prediction of these 1000 randomized  $M_j^\Sigma$  distributions, and the root-mean-square of the 1000 predictions is considered as the uncertainty due to the statistical fluctuation of jet mass templates and the jet mass randomization.

Second, the  $p_T$  bin width used to create jet mass templates is finite, and the jet mass template has a residual  $p_T$ -dependence in the same  $p_T$  bin. The corresponding residual  $p_T$ -dependence uncertainty is estimated by creating predicted  $M_j^\Sigma$  distribution with intentionally mismatched jet kinematics and jet mass templates. For example, for a jet with  $p_T = 300$  GeV, the jet mass template from  $293 \text{ GeV} < p_T < 329$  GeV should be used. Instead, the jet mass template from  $329 \text{ GeV} < p_T < 364$  GeV (or  $270 \text{ GeV} < p_T < 293$  GeV) is applied. The resulting  $M_j^\Sigma$  distribution demonstrates the maximum effect of the residual  $p_T$ -dependence uncertainty.

Third, the background estimation method is exercised in multi-jet Monte Carlo samples, and the difference between predicted and truth background yields is considered as a non-closure uncertainty for the jet mass template method. This non-closure uncertainty covers various other potential systematic uncertainties. The differences found in the PYTHIA and SHERPA samples are consistent within statistical error, and the uncertainty derived from the PYTHIA sample is used due to the larger number of simulated events. The non-closure uncertainty derived from events with four or more large- $R$  jets is also applied to events with five or more large- $R$  jets, where the the Monte Carlo statistics is limited.

The potential bias on the background prediction due to signal contamination is studied with a Monte Carlo-based signal injection test. When the level of signal contamination is comparable to that predicted by signals of gluino direct or cascade decay models not yet excluded by Run-1, the predicted  $M_j^\Sigma$  distribution

is insensitive to the contamination and shows good agreement with the background-only  $M_J^\Sigma$  distribution. If the level of signal contamination is significantly larger than that predicted by the benchmark signal models, an overestimation of background may appear. However, the predicted  $M_J^\Sigma$  distribution is still well below the  $M_J^\Sigma$  distribution of injected signal plus background, indicating that an excess of large signal will not be hidden by the overestimation.

Possible effects induced in the background estimation by the presence of massive objects from top pair production are not explicitly addressed by the background estimation strategy. However, a study similar to the one just described is performed to understand the potential effect of underestimating the contribution from  $t\bar{t}$  background, and the background prediction is found to be insensitive to  $t\bar{t}$  contamination as large as 3 times its theoretical prediction.

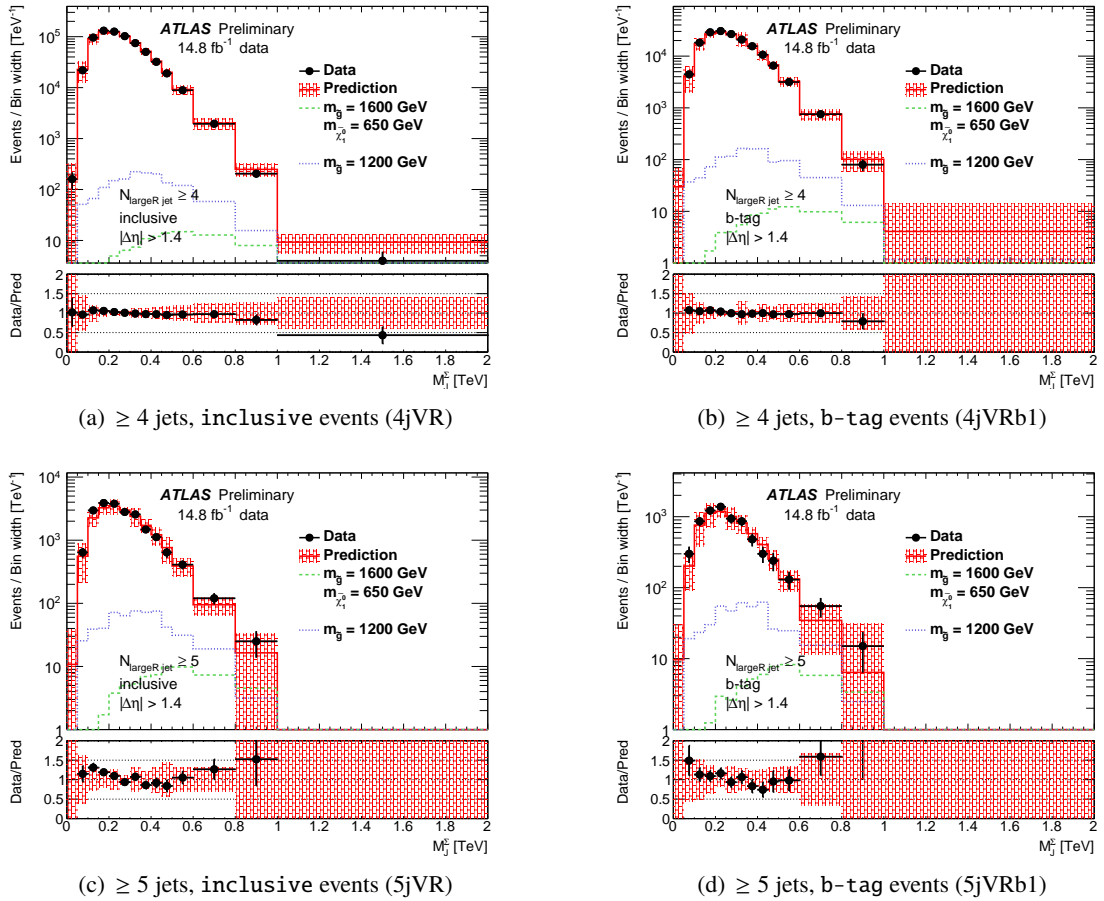


Figure 3: Predicted (solid line) and observed (dots)  $M_J^\Sigma$  distributions for validation regions 4jVR (a), 4jVRb1 (b), 5jVR (c), and 5jVRb1 (d). The shaded area surrounding the predicted  $M_J^\Sigma$  distribution represents the systematic uncertainty of the background estimation. The predicted  $M_J^\Sigma$  distribution is normalized to data in  $0.2 \text{ TeV} < M_J^\Sigma < 0.6 \text{ TeV}$ , where expected contamination from signals of gluino direct or cascade decay models not excluded by the Run-1 analysis [20] is negligible compared to the background statistical uncertainty. The expected contribution from two RPV signal samples are also shown.

The jet mass template method is applied to data. The background estimation performance is first examined in the validation regions. Figure 3 shows the predicted and observed  $M_J^\Sigma$  distributions in the validation regions, where in general a good agreement between the prediction and observation is seen. The modeling

of individual jet mass distribution is also checked for leading, subleading, third leading and fourth leading jets, separately for central jets ( $|\eta| < 1.0$ ) and forward jets ( $|\eta| > 1.0$ ), using events in the 4-jet validation regions (4jVR and 4jVRb1). No sign of mismodeling is found. Figure 4 shows the predicted and observed  $M_J^\Sigma$  distributions in signal regions.

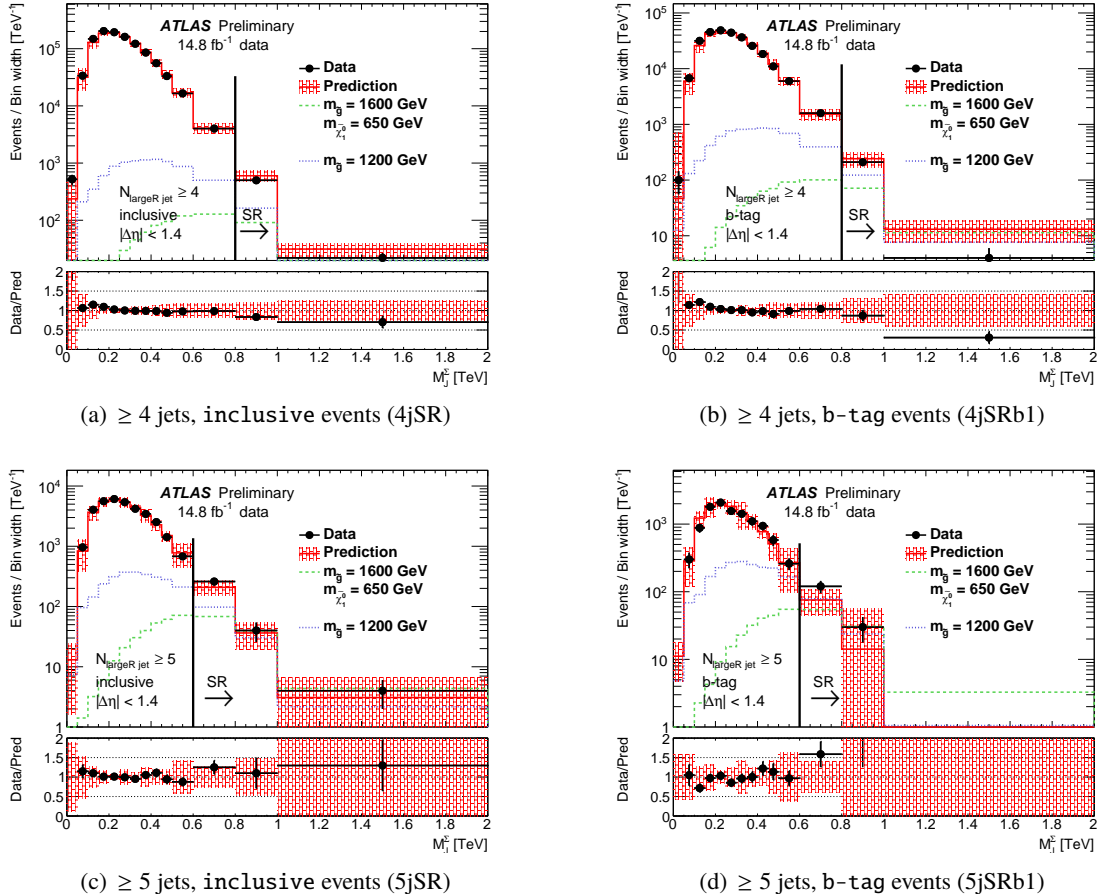


Figure 4: Predicted (solid line) and observed (dots)  $M_J^\Sigma$  distributions for signal regions 4jSR (a), 4jSRb1 (b), 5jSR (c), and 5jSRb1 (d). The shaded area surrounding the predicted  $M_J^\Sigma$  distribution represents the systematic uncertainty of background estimation. The predicted  $M_J^\Sigma$  distribution is normalized to data in  $0.2 \text{ TeV} < M_J^\Sigma < 0.6 \text{ TeV}$ , where expected contamination from signals of gluino direct or cascade decay models not excluded by the Run-1 analysis [20] is negligible compared to the background statistical uncertainty. The expected contribution from two RPV signal samples are also shown.

Many tests are performed using the control regions as well as validation regions in order to determine the robustness of the method. These tests include creating separate jet mass templates for different types of jets (leading, subleading, etc.), applying jet mass templates created from control regions without additional soft large- $R$  jet requirement to validation regions with different jet multiplicities, creating separate jet mass templates for large- $R$  jets that can be matched to a  $b$ -jet and large- $R$  jets that cannot be matched to a  $b$ -jet, varying the  $p_T$  and  $\eta$  binning of the control samples, and varying the binning of jet mass templates. The predicted  $M_J^\Sigma$  distribution is compared to the observed one in both signal and control regions in these tests. It is found that the variation in the predicted yield is within the estimated uncertainties.

The statistical interpretation is based on the event yield in a signal region beyond an  $M_J^\Sigma$  threshold. For

5jSR and 5jSRb1, the threshold used on  $M_J^\Sigma$  is 0.6 TeV, while it is 0.8 TeV for 4jSR and 4jSRb1. These thresholds were found to give the maximum sensitivity to both gluino direct and cascade decay models. The model-dependent interpretation uses data in the 5jSRb1 with  $M_J^\Sigma > 0.6$  TeV, which has the best sensitivity among four signal regions.

## 6 Signal systematic uncertainties

The main systematic uncertainties for the predicted signal yield include the large- $R$  jet mass scale and resolution uncertainties,  $b$ -tagging uncertainty, Monte Carlo statistical uncertainty, and luminosity uncertainty. The large- $R$  jet mass scale and resolution uncertainty is as large as 24% for signal models with  $m_{\tilde{g}} = 1000$  GeV, and drops to  $\approx 8\%$  for signal models with  $m_{\tilde{g}} = 1800$  GeV. The Monte Carlo samples reproduce the b-tagging efficiency measured in data with limited accuracy. Dedicated correction factors, derived from a comparison between data and MC in  $t\bar{t}$  events, are applied to the signal samples. The uncertainty of the correction factors is propagated to a systematic uncertainty on the yields in the signal region. This uncertainty is at around 3% level for all signal models considered in this analysis. Due to low acceptance, the statistical uncertainty of the signal yield predicted by the Monte Carlo samples can be as large as 8% for signal models with  $m_{\tilde{g}} \leq 1000$  GeV. The Monte Carlo statistical uncertainty for signal models with large  $m_{\tilde{g}}$  is negligible.

Uncertainties on the signal acceptance due to the choices of PDF, QCD scales and the modeling of initial state radiation (ISR) are studied. The uncertainty of PDF and QCD scales is found to be up to 20% for  $m_{\tilde{g}} \approx 1000$  GeV, and a few percent for  $m_{\tilde{g}} \approx 1600$  GeV. Since the signal samples are generated at the leading order, the ISR modeling uncertainty is evaluated by varying  $\alpha_s$  used in the Pythia parton showering up and down by 10 %. This uncertainty is found to be up to 10 % at around  $m_{\tilde{g}} = 1000$  GeV, and a few percent at around  $m_{\tilde{g}} = 1600$  GeV and beyond.

## 7 Results

Table 2 summarizes the predicted and observed event yields in signal regions with different  $M_J^\Sigma$  cuts. No excess is seen in the  $\geq 4$  jets signal regions (4jSR and 4jSRb1), and small excesses are seen in  $\geq 5$  jets signal regions (5jSR and 5jSRb1).

The predicted and observed event yields shown in Table 2 are used to construct a likelihood function, where signal and background systematic uncertainties are incorporated as nuisance parameters. A likelihood function is constructed with the observed and predicted yields shown in Table 2, with signal and background systematic uncertainties incorporated as nuisance parameters. A frequentist procedure based on the profile likelihood ratio [61] is used to evaluate the  $p_0$ -values of these excesses, and the results are shown in Table 3. Since no significant excess is seen in any of the signal regions, a model-independent limit on  $\sigma_{\text{vis}}$ , defined as the cross section times acceptance times efficiency of a generic BSM model, is calculated using the modified frequentist  $CL_s$  method [62]. The observed and expected limits are also shown in Table 3.

Limits are also set on the production of RPV signals in the context of gluino direct and cascade decay models and are shown in Figure 5. Typically, for RPV signals from the gluino cascade decay model with  $m_{\tilde{g}} \geq 1000$  GeV, the ratio of the detector level acceptance over truth level acceptance is between 0.95 and 1.10, for 4jSR with  $M_J^\Sigma > 0.8$  TeV and 5jSR with  $M_J^\Sigma > 0.6$  TeV. For signal regions with  $b$ -tagging

Region	$M_j^\Sigma$ cut	observed	SM predicted	$m_{\tilde{g}} = 1600$ GeV $m_{\tilde{\chi}_1^0} = 650$ GeV	$m_{\tilde{g}} = 1200$ GeV
4jSRb1	$> 0.8$ TeV	46	$61 \pm 10 \pm 6 \pm 12$	$25.6 \pm 2.8$	$32.4 \pm 6.0$
4jSR		122	$151 \pm 15 \pm 17 \pm 20$	$32.9 \pm 3.0$	$43.6 \pm 4.0$
5jSRb1	$> 0.6$ TeV	30	$18.2 \pm 4.2 \pm 2.5 \pm 3.0$	$20.2 \pm 2.3$	$21.6 \pm 5.0$
5jSR		64	$51.4 \pm 7.7 \pm 7.2 \pm 6.5$	$25.9 \pm 2.8$	$27.6 \pm 5.6$

Table 2: Observed and predicted yields in signal regions with various  $M_j^\Sigma$  cuts. The three uncertainty components of the background prediction are the template and jet mass randomization statistical uncertainty, residual  $p_T$ -dependence uncertainty and the Monte Carlo-based non-closure uncertainty. The predicted signal yields of a gluino cascade decay model ( $m_{\tilde{g}} = 1600$  GeV,  $m_{\tilde{\chi}_1^0} = 650$  GeV) and a gluino direct decay model ( $m_{\tilde{g}} = 1200$  GeV), and their experimental and Monte Carlo statistical uncertainties, are also shown.

Signal Region	$M_j^\Sigma$ cut	Expected limit (fb)	Observed Limit (fb)	$p_0$ -value
4jSRb1	$> 0.8$ TeV	$2.50^{+1.22}_{-0.74}$	1.76	0.82
4jSR		$4.40^{+2.16}_{-1.29}$	3.11	0.84
5jSRb1	$> 0.6$ TeV	$1.08^{+0.47}_{-0.30}$	2.00	0.06
5jSR		$2.03^{+1.12}_{-0.57}$	2.94	0.21

Table 3: Expected and observed limits on the signal production cross-section for the four signal regions, and  $p_0$ -values of excesses in the 5-jet signal regions.

requirements, 5jSRb1 with  $M_j^\Sigma > 0.6$  TeV and 4jSRb1 with  $M_j^\Sigma > 0.8$  TeV, this ratio drops to  $\approx 0.75 - 0.98$  for signal models with  $m_{\tilde{\chi}_1^0} \geq 250$  GeV, and it is further reduced to  $\approx 0.65 - 0.75$ , for signal models with small  $m_{\tilde{\chi}_1^0}$  (e.g.,  $m_{\tilde{\chi}_1^0} <$  top mass), due to  $b$ -jets in signal events having higher  $p_T$  for which the  $b$ -tagging is less efficient. With  $14.8 \text{ fb}^{-1}$  at  $\sqrt{s} = 13$  TeV, the search has excluded a gluino with mass up to 1050 GeV - 1550 GeV in the gluino cascade decay model, with the most stringent limit achieved at around  $m_{\tilde{\chi}_1^0} \geq 800$  GeV and the weakest limit achieved at around  $m_{\tilde{\chi}_1^0} \geq 50$  GeV; for the gluino direct decay model, the search has excluded a gluino with mass up to 1080 GeV.

## 8 Conclusion

A search for  $R$ -Parity Violating SUSY signals in events with multiple jets is conducted. Distributions of events as a function of total jet mass are examined. No significant excess is seen in any signal regions. Limits are set on the production of gluinos in the gluino direct and cascade decay models in the UDD scenarios of RPV SUSY. In the gluino cascade decay model, gluinos with masses up to 1000 GeV - 1550 GeV are excluded, depending on the neutralino mass; in the gluino direct decay model, gluinos with masses up to 1080 GeV are excluded. Model-independent limits are also set on the signal production cross-section in four overlapping signal regions. These significantly extend the limits from the 8 TeV LHC analyses.

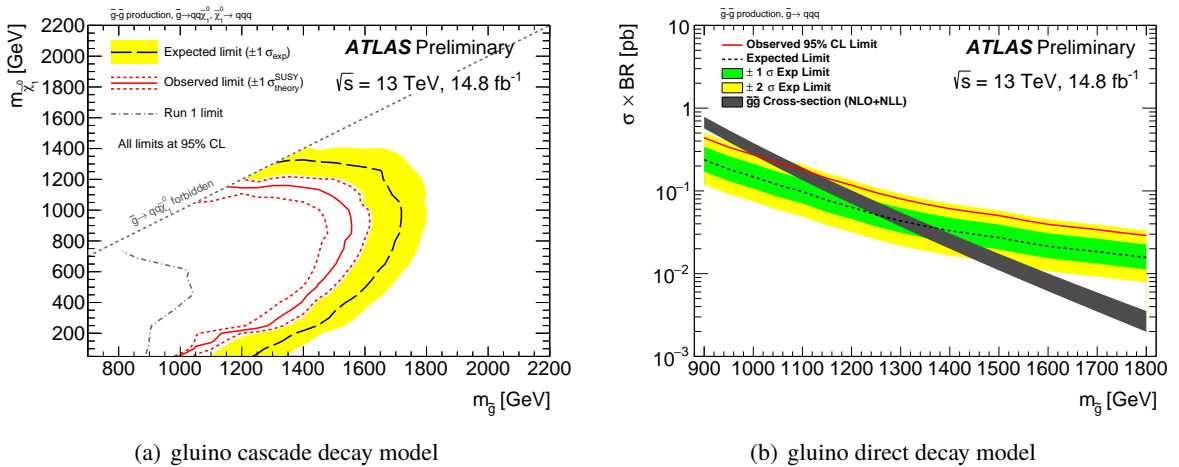


Figure 5: (a) Expected and observed exclusion limits in the  $(m_{\tilde{g}}, m_{\tilde{\chi}_1^0})$  plane for the gluino cascade decay model. Limits are obtained by using the signal region with the best expected sensitivity for every signal point (5jSRb1 with  $M_{\text{J}}^{\Sigma} > 0.6$  TeV). The dashed black lines show the expected limits at 95% CL, with the light (yellow) bands indicating the  $1\sigma$  excursions due to experimental uncertainties. Observed limits are indicated by medium dark (maroon) curves, where the solid contour represents the nominal limit, and the dotted lines are obtained by varying the signal cross-section by the renormalization and factorization scale and PDF uncertainties. The observed limit from the Run-1 analysis [20] is also shown as a solid line. (b) Expected and observed cross-section limits for the gluino direct decay model gluino models.

## References

- [1] Y. A. Gol'fand and E. P. Likhtman, *Extension of the Algebra of Poincare Group Generators and Violation of  $p$  Invariance*, JETP Lett. **13** (1971) 323, [Pisma Zh.Eksp.Teor.Fiz.13:452-455,1971].
- [2] D. V. Volkov and V. P. Akulov, *Is the Neutrino a Goldstone Particle?*, Phys. Lett. **B46** (1973) 109.
- [3] J. Wess and B. Zumino, *Supergauge Transformations in Four-Dimensions*, Nucl. Phys. **B70** (1974) 39.
- [4] J. Wess and B. Zumino, *Supergauge Invariant Extension of Quantum Electrodynamics*, Nucl. Phys. **B78** (1974) 1.
- [5] S. Ferrara and B. Zumino, *Supergauge Invariant Yang-Mills Theories*, Nucl. Phys. **B79** (1974) 413.
- [6] A. Salam and J. A. Strathdee, *Supersymmetry and Nonabelian Gauges*, Phys. Lett. **B51** (1974) 353.
- [7] R. Barbieri and G. F. Giudice, *Upper Bounds on Supersymmetric Particle Masses*, Nucl. Phys. **B306** (1988) 63.
- [8] B. de Carlos and J. A. Casas, *One loop analysis of the electroweak breaking in supersymmetric models and the fine tuning problem*, Phys. Lett. **B309** (1993) 320, arXiv: [hep-ph/9303291 \[hep-ph\]](#).
- [9] G. R. Farrar and P. Fayet, *Phenomenology of the Production, Decay, and Detection of New Hadronic States Associated with Supersymmetry*, Phys. Lett. **B76** (1978) 575.
- [10] L. J. Hall and M. Suzuki, *Explicit R-Parity Breaking in Supersymmetric Models*, Nucl. Phys. **B231** (1984) 419.
- [11] G. G. Ross and J. W. F. Valle, *Supersymmetric Models Without R-Parity*, Phys. Lett. **B151** (1985) 375.
- [12] V. D. Barger, G. F. Giudice and T. Han, *Some New Aspects of Supersymmetry R-Parity Violating Interactions*, Phys. Rev. **D40** (1989) 2987.
- [13] H. K. Dreiner, *An Introduction to explicit R-parity violation*, (1997), [Adv. Ser. Direct. High Energy Phys.21,565(2010)], arXiv: [hep-ph/9707435 \[hep-ph\]](#).
- [14] R. Barbier et al., *R-parity violating supersymmetry*, Phys. Rept. **420** (2005) 1, arXiv: [hep-ph/0406039 \[hep-ph\]](#).
- [15] H. K. Dreiner, *An introduction to explicit R-parity violation*, Pramana **51** (1998) 123, arXiv: [hep-ph/9707435v2 \[hep-ph\]](#).
- [16] B. Allanach, A. Dedes and H. Dreiner, *R parity violating minimal supergravity model*, Phys. Rev. **D69** (2004) 115002, arXiv: [hep-ph/0309196 \[hep-ph\]](#).
- [17] E. Nikolidakis and C. Smith, *Minimal Flavor Violation, Seesaw, and R-parity*, Phys. Rev. **D77** (2008) 015021, arXiv: [0710.3129 \[hep-ph\]](#).
- [18] C. Csaki, Y. Grossman and B. Heidenreich, *MFV SUSY: A Natural Theory for R-Parity Violation*, Phys. Rev. **D85** (2012) 095009, arXiv: [1111.1239 \[hep-ph\]](#).

[19] The ATLAS Collaboration, *Search for pair production of massive particles decaying into three quarks with the ATLAS detector in  $\sqrt{s} = 7$  TeV  $pp$  collisions at the LHC*, **JHEP** **12** (2012) 086, arXiv: [1210.4813](https://arxiv.org/abs/1210.4813) [hep-ex].

[20] The ATLAS Collaboration, *Search for massive supersymmetric particles decaying to many jets using the ATLAS detector in  $pp$  collisions at  $\sqrt{s} = 8$  TeV*, **Phys. Rev. D** **91** (2015) 112016, [Erratum: *Phys. Rev. D* 93, no. 3, 039901 (2016)], arXiv: [1502.05686](https://arxiv.org/abs/1502.05686) [hep-ex].

[21] The CMS Collaboration, *Searches for  $R$ -parity-violating supersymmetry in  $pp$  collisions at  $\sqrt{s}=8$  TeV in final states with 0-4 leptons*, (2016), arXiv: [1606.08076](https://arxiv.org/abs/1606.08076) [hep-ex].

[22] The ATLAS Collaboration, *The ATLAS Experiment at the CERN Large Hadron Collider*, **JINST** **3** (2008) S08003.

[23] M Capeans et al., *ATLAS Insertable B-Layer Technical Design Report*, (2010), ATLAS-TDR-19, URL: <http://cds.cern.ch/record/1291633>.

[24] The ATLAS Collaboration, *2015 start-up trigger menu and initial performance assessment of the ATLAS trigger using Run-2 data*, (2016), ATL-DAQ-PUB-2016-001, URL: <http://cds.cern.ch/record/2136007>.

[25] J. Alwall et al., *The automated computation of tree-level and next-to-leading order differential cross sections, and their matching to parton shower simulations*, **JHEP** **07** (2014) 079, arXiv: [1405.0301](https://arxiv.org/abs/1405.0301) [hep-ph].

[26] T. Sjöstrand et al., *An Introduction to PYTHIA 8.2*, **Comput. Phys. Commun.** **191** (2015) 159, arXiv: [1410.3012](https://arxiv.org/abs/1410.3012) [hep-ph].

[27] The ATLAS Collaboration, *Summary of ATLAS Pythia 8 tunes*, (2012), ATL-PHYS-PUB-2012-003, URL: <http://cds.cern.ch/record/1474107>.

[28] R. D. Ball et al., *Parton distributions with LHC data*, **Nucl. Phys.** **B867** (2013) 244, arXiv: [1207.1303](https://arxiv.org/abs/1207.1303) [hep-ph].

[29] D. J. Lange, *The EvtGen particle decay simulation package*, **Nucl. Instrum. Meth.** **A462** (2001) 152.

[30] T. Gleisberg et al., *Event generation with SHERPA 1.1*, **JHEP** **02** (2009) 007, arXiv: [0811.4622](https://arxiv.org/abs/0811.4622) [hep-ph].

[31] W. Beenakker et al., *Squark and gluino production at hadron colliders*, **Nucl. Phys.** **B492** (1997) 51, arXiv: [hep-ph/9610490](https://arxiv.org/abs/hep-ph/9610490) [hep-ph].

[32] A. Kulesza and L. Motyka, *Threshold resummation for squark-antisquark and gluino-pair production at the LHC*, **Phys. Rev. Lett.** **102** (2009) 111802, arXiv: [0807.2405](https://arxiv.org/abs/0807.2405) [hep-ph].

[33] A. Kulesza and L. Motyka, *Soft gluon resummation for the production of gluino-gluino and squark-antisquark pairs at the LHC*, **Phys. Rev. D** **80** (2009) 095004, arXiv: [0905.4749](https://arxiv.org/abs/0905.4749) [hep-ph].

[34] W. Beenakker et al., *Soft-gluon resummation for squark and gluino hadroproduction*, **JHEP** **12** (2009) 041, arXiv: [0909.4418](https://arxiv.org/abs/0909.4418) [hep-ph].

[35] W. Beenakker et al., *Squark and Gluino Hadroproduction*, **Int. J. Mod. Phys. A** **26** (2011) 2637, arXiv: [1105.1110](https://arxiv.org/abs/1105.1110) [hep-ph].

[36] C. Borschensky et al.,  
*Squark and gluino production cross sections in pp collisions at  $\sqrt{s} = 13, 14, 33$  and  $100$  TeV*, *Eur. Phys. J. C* **74** (2014) 3174, arXiv: [1407.5066 \[hep-ph\]](#).

[37] S. Schumann and F. Krauss,  
*A Parton shower algorithm based on Catani-Seymour dipole factorisation*, *JHEP* **0803** (2008) 038, arXiv: [0709.1027 \[hep-ph\]](#).

[38] S. Hoeche et al., *QCD matrix elements and truncated showers*, *JHEP* **0905** (2009) 053, arXiv: [0903.1219 \[hep-ph\]](#).

[39] H.-L. Lai et al., *New parton distributions for collider physics*, *Phys. Rev. D* **82** (2010) 074024, arXiv: [1007.2241 \[hep-ph\]](#).

[40] S. Alioli et al., *A general framework for implementing NLO calculations in shower Monte Carlo programs: the POWHEG BOX*, *JHEP* **06** (2010) 043, arXiv: [1002.2581 \[hep-ph\]](#).

[41] T. Sjostrand, S. Mrenna and P. Z. Skands, *PYTHIA 6.4 physics and manual*, *JHEP* **0605** (2006) 026, arXiv: [0603175 \[hep-ph\]](#).

[42] J. Pumplin et al.,  
*New generation of parton distributions with uncertainties from global QCD analysis*, *JHEP* **07** (2002) 012, arXiv: [hep-ph/0201195 \[hep-ph\]](#).

[43] P. Z. Skands, *Tuning Monte Carlo Generators: The Perugia Tunes*, *Phys. Rev. D* **82** (2010) 074018, arXiv: [1005.3457 \[hep-ph\]](#).

[44] S. Agostinelli et al., *GEANT4: A Simulation toolkit*, *Nucl. Instrum. Meth. A* **506** (2003) 250.

[45] The ATLAS Collaboration, *The ATLAS Simulation Infrastructure*, *Eur. Phys. J. C* **70** (2010) 823, arXiv: [1005.4568 \[physics.ins-det\]](#).

[46] The ATLAS Collaboration,  
*The simulation principle and performance of the ATLAS fast calorimeter simulation FastCaloSim*, (2010), ATL-PHYS-PUB-2010-013, URL: <http://cds.cern.ch/record/1300517>.

[47] The ATLAS Collaboration, *Improved luminosity determination in pp collisions at  $\sqrt{s} = 7$  TeV using the ATLAS detector at the LHC*, *Eur. Phys. J. C* **73** (2013) 2518, arXiv: [1302.4393 \[hep-ex\]](#).

[48] M. Cacciari, G. P. Salam and G. Soyez, *The Anti- $k(t)$  jet clustering algorithm*, *JHEP* **04** (2008) 063, arXiv: [0802.1189 \[hep-ph\]](#).

[49] The ATLAS Collaboration,  
*Topological cell clustering in the ATLAS calorimeters and its performance in LHC Run 1*, (2016), arXiv:1603.02934. CERN-PH-EP-2015-304, URL: <http://cds.cern.ch/record/2138166>.

[50] T Barillari et al., *Local Hadronic Calibration*, (2008), ATL-LARG-PUB-2009-001-2. ATL-COM-LARG-2008-006. ATL-LARG-PUB-2009-001, URL: <http://cds.cern.ch/record/1112035>.

[51] S. Catani et al., *Longitudinally invariant  $K_t$  clustering algorithms for hadron hadron collisions*, *Nucl. Phys. B* **406** (1993) 187.

[52] The ATLAS Collaboration, *Performance of jet substructure techniques for large- $R$  jets in proton-proton collisions at  $\sqrt{s} = 7$  TeV using the ATLAS detector*, *JHEP* **09** (2013) 076, arXiv: [1306.4945 \[hep-ex\]](#).

- [53] D. Krohn, J. Thaler and L.-T. Wang, *Jet Trimming*, **JHEP** **02** (2010) 084, arXiv: [0912.1342 \[hep-ph\]](#).
- [54] The ATLAS Collaboration, *Jet energy measurement with the ATLAS detector in proton-proton collisions at  $\sqrt{s} = 7$  TeV*, **Eur. Phys. J.** **C73** (2013) 2304, arXiv: [1112.6426 \[hep-ex\]](#).
- [55] G. Aad et al., *Performance of b-Jet Identification in the ATLAS Experiment*, **JINST** **11** (2016) P04008, arXiv: [1512.01094 \[hep-ex\]](#).
- [56] The ATLAS Collaboration, *Optimisation of the ATLAS b-tagging performance for the 2016 LHC Run*, (2016), URL: <http://cds.cern.ch/record/2160731>.
- [57] A. Hook et al., *High Multiplicity Searches at the LHC Using Jet Masses*, **JHEP** **3** (2012) 9, arXiv: [1202.0558](#).
- [58] S. El Hedri et al., *Learning How to Count: A High Multiplicity Search for the LHC*, **JHEP** **08** (2013) 136, arXiv: [1302.1870](#).
- [59] T. Cohen et al., *Jet Substructure Templates: Data-driven QCD Backgrounds for Fat Jet Searches*, **JHEP** **05** (2014) 005, arXiv: [1402.0516 \[hep-ph\]](#).
- [60] The ATLAS Collaboration, *Search for new phenomena in final states with large jet multiplicities and missing transverse momentum at  $\sqrt{s}=8$  TeV proton-proton collisions using the ATLAS experiment*, **JHEP** **10** (2013) 130, [Erratum: **JHEP**01,109(2014)], arXiv: [1308.1841 \[hep-ex\]](#).
- [61] The ATLAS and CMS Collaborations, *Procedure for the LHC Higgs boson search combination in summer 2011*, (2011), CMS-NOTE-2011-005. ATL-PHYS-PUB-2011-11, URL: <http://cds.cern.ch/record/1379837>.
- [62] A. L. Read, *Presentation of search results: the  $CL_s$  technique*, **Journal of Physics G: Nuclear and Particle Physics** **28** (2002) 2693, URL: <http://stacks.iop.org/0954-3899/28/i=10/a=313>.

	Gluino cascade (via $\tilde{\chi}_1^0$ ) [ $\tilde{g}, \tilde{\chi}_1^0$ ] : [1600, 650] [GeV]	Gluino direct $\tilde{g}$ : 1100 [GeV]
Trigger $p_T^{lead} > 440 GeV$	120 119	2401 2236
$n_{jet} \geq 4$	97.1	1159
$M_J^\Sigma > 0.8 \text{ TeV}$	35.4	63.3
$ \Delta\eta_{12}  < 1.4$	33.0	56.6
b-tag	25.7	43.3
$n_{jet} \geq 5$	50.2	296
$M_J^\Sigma > 0.6 \text{ TeV}$	28.7	41.6
$ \Delta\eta_{12}  < 1.4$	25.9	35.0
b-tag	20.3	26.7

Table 4: Cutflow for two supersymmetric models. For the gluino cascade decay model, with 1600 GeV gluinos and 650 GeV neutralinos, 20000 events were generated. For the gluino direct decay model, with 1100 GeV gluinos, 40000 events were generated.

## Appendix

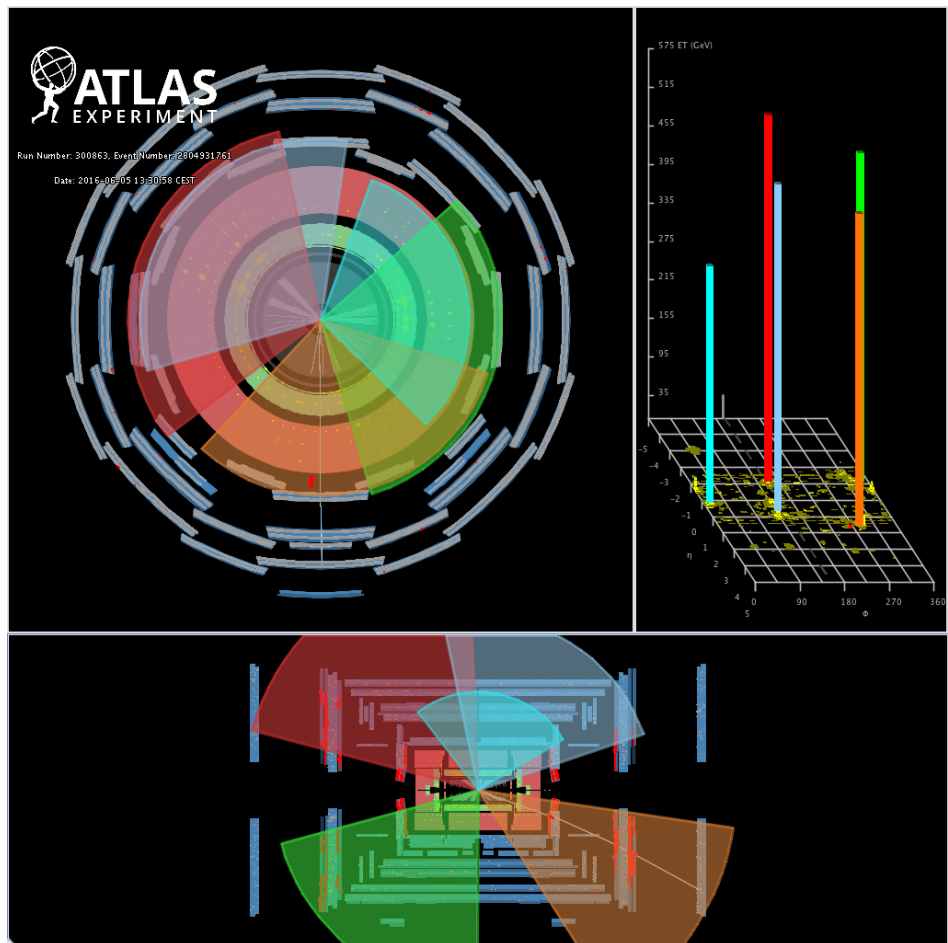


Figure 6: Event display showing a b-tag event with 5 large- $R$  jet and  $M_j^\Sigma = 0.62$  TeV.

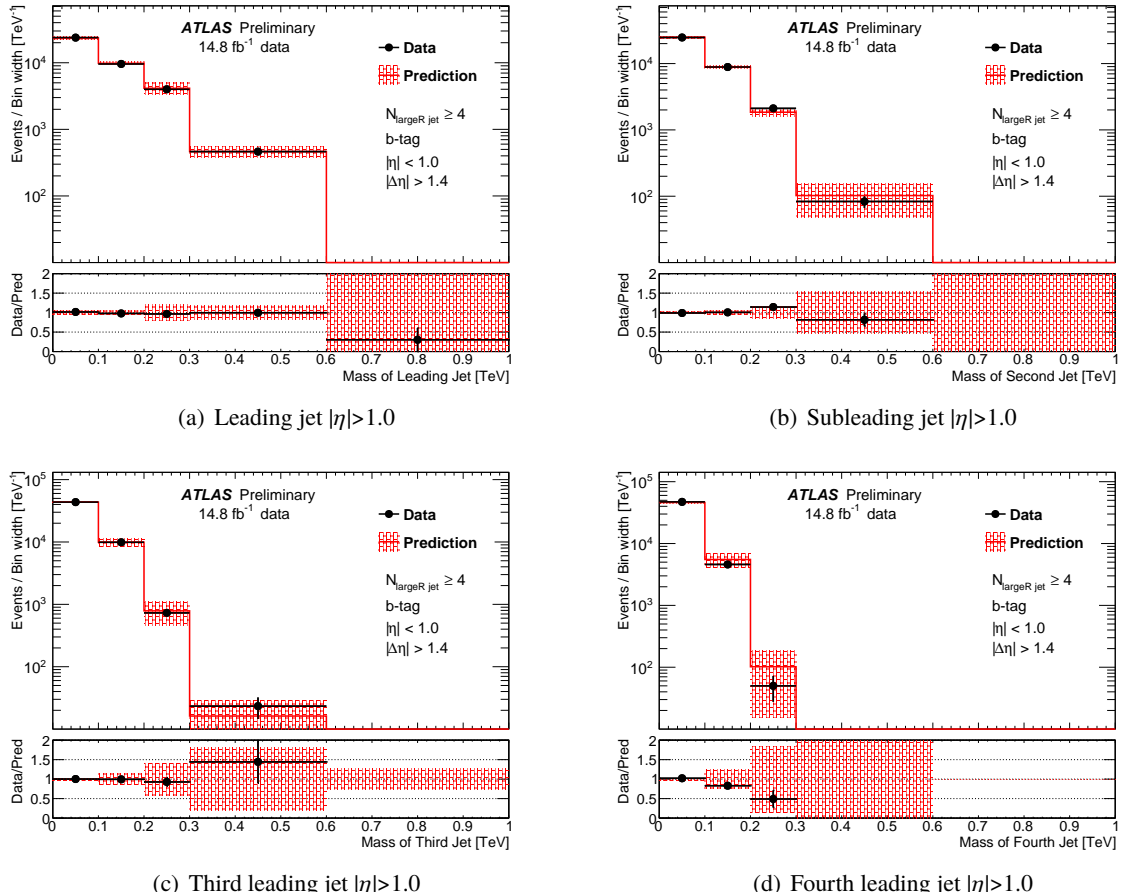


Figure 7: Predicted (solid line) and observed (dots) individual jet mass distributions for leading jet(??), subleading jet(??), third leading jet(??), and fourth leading jet(??) with a  $|\eta| < 1.0$  requirement in validation region 4jVRb1. The shaded area around the predicted  $M_j^\Sigma$  distribution indicates the systematic uncertainty of the prediction.

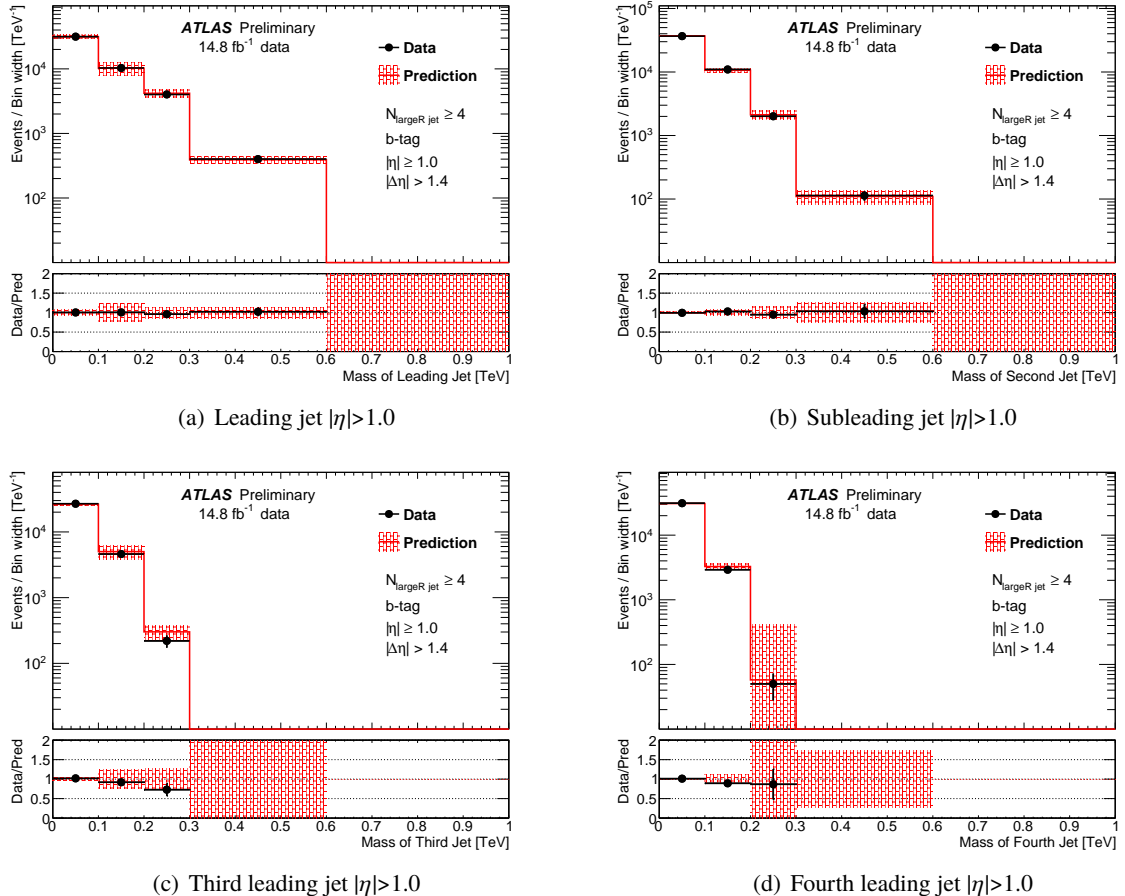


Figure 8: Predicted (solid line) and observed (dots) individual jet mass distributions for leading jet((a)), subleading jet((b)), third leading jet((c)), and fourth leading jet((d)) with a  $|\eta| < 1.0$  requirement in validation region 4jVRb1. The shaded area around the predicted  $M_j^\Sigma$  distribution indicates the systematic uncertainty of the prediction.